Available online at www.sciencedirect.com
SCIENCE DIRECT®
Combustion and Flame 137 (2004) 320–339
Combustion and Flame
www.elsevier.com/locate/jnlabr/cnf

Effects of strain rate on high-pressure nonpremixed *n*-heptane autoignition in counterflow

Shiling Liu,[a,*] John C. Hewson,[a] Jacqueline H. Chen,[a] and Heinz Pitsch [b]

[a] *Reacting Flow Research Department, Combustion Research Facility, Sandia National Laboratories, P.O. Box 969, MS 9051, Livermore, CA 94551-0969, USA*

[b] *Center for Turbulence Research, Stanford University, Stanford, CA 94305-3030, USA*

Received 18 June 2003; received in revised form 7 December 2003; accepted 20 January 2004

Abstract

The effect of steady strain on the transient autoignition of *n*-heptane at high pressures is studied numerically with detailed chemistry and transport in a counterflow configuration. Skeletal and reduced *n*-heptane mechanisms are developed and validated against experiments over a range of pressure and stoichiometries. Two configurations are investigated using the skeletal mechanism. First, the effect of strain rate on multistage *n*-heptane ignition is studied by imposing a uniform temperature for both the fuel and the oxidizer streams. Second, a temperature gradient between the fuel and the oxidizer streams is imposed. The global effect of strain on ignition is captured by a Damköhler number based on either the heat-release rate or the characteristic chain-branching rate. Results show that for low to moderate strain rates, both the low- and intermediate-temperature chemistries evolve in a manner comparable to that in homogeneous systems, including the negative temperature coefficient regime, but with somewhat slower evolution attributable to diffusive losses. At high strain rates diffusive losses inhibit ignition; for two-stage ignition, it is found that ignition is inhibited during the second, intermediate-temperature stage. The imposition of an overall temperature gradient further inhibits ignition because reaction zones for key branching reactions with large activation energies are narrowed. For a fixed oxidizer stream temperature that is not sufficiently high, a higher fuel temperature results in a shorter ignition delay provided that the heptyl radicals are mainly oxidized by low-temperature chemistry. As expected, an increase in pressure significantly increases reaction rates and reduces ignition delay time. However, with increasing pressure there is a shift toward single-stage low-temperature-dominated ignition which serves to delay ignition.

Keywords: *n*-Heptane; Autoignition; Counterflow; Nonpremixed; Strain effect

1. Introduction

Ignition processes are an integral part of combustion in many practical systems including, for example, diesel engines. Ignition in diesel engines typically occurs while strong fuel–air and temperature inhomogeneities exist, making the study of ignition in nonpremixed configurations with compressed reactants particularly valuable. *n*-Heptane has a cetane number (CN ≈ 56) similar to that of diesel fuel (CN ≈ 50), and it is widely used as a model fuel to study the ignition process. Research into *n*-heptane ignition in homogeneous systems, where kinetics is best studied, has progressed nicely [1–11], but there have been few fundamental studies of inhomogeneous mixtures at conditions relevant to diesel ignition. The current work seeks to provide a better understanding of the transient ignition process in such systems. More

* Corresponding author.
E-mail address: sliu@sandia.gov (S. Liu).

0010-2180/$ – see front matter
doi:10.1016/j.combustflame.2004.01.011

specifically, the effects of fuel–air gradients and temperature gradients on the ignition process are studied. The key chemical behavior that distinguishes ignition under the present diesel-like conditions from that under other conditions is the combined effect of so-called low-temperature and intermediate-temperature chemistry on the ignition process. It is known that for homogeneous *n*-heptane–air mixtures ignition can occur in a multistage mode [1] where both low- and intermediate-temperature chemistries play a role. The different chemistry regimes are defined in later sections and Refs. [3] and [4] provide details of these processes.

Ignition in inhomogeneous systems with highly simplified chemistry has been studied for some time [12,13] and has recently been studied in the context of detailed chemical mechanisms. Blouch and Law [14] studied the effects of strain and pressure on the air temperature required to autoignite *n*-heptane in steady-state counterflow systems. Seiser et al. [15] studied strain effects on extinction and autoignition in a steady-state counterflow configuration at one atmosphere. Sreedhara and Lakshmisha [16] studied the autoignition of *n*-heptane in an initially nonpremixed medium under isotropic, homogeneous, and decaying turbulence environment using direct numerical simulation. Measurements and analysis in these studies were conducted at temperatures sufficiently high that the low-temperature chemistry was of little importance. Schnaubelt et al. [17] studied *n*-heptane droplet ignition in microgravity at temperatures and pressures suitable for observing the multistage autoignition process. Pitsch and Peters [18] numerically investigated the autoignition of *n*-heptane under diesel engine conditions using a flamelet model in conjunction with CFD simulations and proposed a formulation of ignition delay time under strained conditions as a function of scalar dissipation rate and homogeneous ignition delay time for a fixed fuel temperature of 400 K at 40 to 50 bars. In these studies the strain rate (or scalar dissipation rate) was identified as tending to inhibit ignition, as do lower boundary temperatures and pressures. In recent work, Gopalakrishnan and Abraham [19] have numerically investigated the role of differential diffusion in *n*-heptane ignition and found that differential diffusion effects are most significant for those cases, at lower pressures and temperatures, where ignition delays are longer. Nevertheless, there are no comprehensive studies, to the authors' knowledge, that analyze the effects of inhomogeneities, specifically the gradients associated with those inhomogeneities, on the transient ignition process for temperatures and pressures where both low- and intermediate-temperature chemistries are significant.

Motivated by the need to study transient autoignition processes in CFD that include coupling between transport and reaction, new skeletal and reduced mechanisms for studies of multistage autoignition at high pressures are developed and validated over a wide range of conditions. Seiser et al. [15] had previously developed a short mechanism of 159 species and 770 reversible reactions from a detailed mechanism that includes 2540 reversible elementary reactions among 556 species [3]. However, computing transient ignition with this mechanism is very inefficient. The present skeletal mechanism is much smaller with 43 species and 185 reactions, counting forward and backward reactions individually. The reduced mechanism has 18 global reaction steps.

The first objective of the present study is to examine the effect of strain rate on multistage *n*-heptane ignition between counterflowing fuel and oxidizer streams, each at the same temperature. The second objective is to investigate the effect of strain rate in the presence of an imposed temperature gradient between the fuel and the oxidizer streams. In particular, the temperature gradient considered encompasses the low- to intermediate-temperature ignition kinetics with ignition causing a transition to high-temperature kinetics.

In the following, the skeletal and reduced chemical mechanisms for *n*-heptane ignition and oxidation are presented first. This is followed by an overview of the numerical methods and multistage ignition phenomena. Then the effect of strain rate on ignition delay is discussed for uniform and stratified fuel and oxidizer boundary temperature conditions. Finally the effects of pressure and fuel stream temperature on ignition are examined.

2. Reduced chemical mechanisms for *n*-heptane

The development of the reduced mechanism starts from a detailed kinetic reaction mechanism for the ignition and combustion of *n*-heptane [20]. This mechanism has been revised and updated in the H_2/O_2- and the C_1–C_3-part using recent kinetic rate data from Baulch et al. [21,22]. The detailed mechanism consists of 1008 elementary reactions and 168 chemical species. With the knowledge of the main reaction paths, already described by Pollard [23] and Benson [24], a remarkably shortened mechanism can be derived by neglecting unimportant side chains. This mechanism is referred to as a skeletal mechanism and is the starting point for the further reduction. The resulting skeletal mechanism consists of 43 chemical components and 185 reactions, counting forward and backward reactions individually. The reactions

remaining in the skeletal mechanism and the Arrhenius coefficients are given in Appendix A.

A similar skeletal mechanism has been derived previously by Bollig et al. [25] to predict NO_x precursor species in steady diffusion flames. This reaction set has been included as a subset of the present mechanism to preserve the applicability of the mechanism in pollutant formation calculations.

In addition to the mechanism from Bollig et al. [25], for a proper description of the ignition process, a fuel consumption path over a second heptyl radical is needed. Also some reactions for radical-poor combustion, for instance, some reactions with HO_2 and H_2O_2, have to remain in the mechanism. The low-temperature reaction paths arising by different heptyl isomers have been lumped to only one chain, which is similar to the low-temperature autoignition steps by Cox and Cole [26].

Starting from the skeletal mechanism and introducing steady-state assumptions for intermediate components, which are consumed rapidly as compared to their formation and changes by transport processes, a reduced reaction scheme with 18 global reaction steps can be obtained. These global reactions are given in Table 1 and characterize the main consumption reactions of the species included therein. The reaction rates of the global steps are based on the kinetic rate data of the elementary reactions and can be provided on request.

Reactions I and II are the initiation reactions for high- and low-temperature autoignition, respectively. The low-temperature initiation reaction II reveals the formation of heptylperoxy radicals (RO_2). These react in global step III by internal isomerization reactions, a further O_2 addition, and a first OH abstraction to ketoheptylperoxide $OR''O_2H$. The decomposition of this component in reaction IV, which results in the formation of an OH radical, represents the chain branching in the low-temperature range. Reactions V–XIII describe the consumption of the intermediate component hexene, butene, propene, allene, ethene, acetylene, methane, the methyl radical, and formaldehyde, respectively. Steps XIV and XV lead to the formation of radicals in a very short, radical-poor initiation time, during which the H abstraction by O_2 attack leads to a relatively high amount of hydroperoxy radicals. These reactions also form radicals during ignition at high temperatures. The water gas shift reaction XVI represents the oxidation of CO to CO_2, which occurs during thermal runaway and leads to strong heat release. Reaction XVII is the main radical producing step after ignition occurs, and finally, global reaction XVIII represents chain breaking by recombination reaction.

Table 1
Reduced 18-step mechanism for *n*-heptane

No.	Reactions
I	$n\text{-}C_7H_{16} = C_3H_6 + 2C_2H_4 + H_2$
II	$n\text{-}C_7H_{16} + O_2 + OH = RO_2 + H_2O$
III	$RO_2 + O_2 = OR''O_2H + OH$
IV	$OR''O_2H = 2C_2H_4 + CH_2O + CH_3 + CO + OH$
V	$1\text{-}C_6H_{12} + H_2O = C_3H_6 + C_3H_4 + H_2O$
VI	$1\text{-}C_4H_8 + OH = C_2H_4 + CH_3 + CH_2O$
VII	$C_3H_6 + H_2O = C_2H_4 + CH_2O + H_2$
VIII	$C_3H_4 + H_2O = C_2H_4 + CO + H_2$
IX	$C_2H_4 = C_2H_2 + H_2$
X	$C_2H_2 + O_2 = 2CO + H_2$
XI	$CH_4 + H = CH_3 + H_2$
XII	$CH_3 + OH = CH_2O + H_2$
XIII	$CH_2O = CO + H_2$
XIV	$2HO_2 = H_2O_2 + O_2$
XV	$H_2O_2 = 2OH$
XVI	$CO + H_2O = CO_2 + H_2$
XVII	$O_2 + H_2 = 2OH$
XVIII	$2H = H_2$

In the following we show comparisons of results from the skeletal and the reduced mechanism with measured data from various experiments. A comparison of autoignition delay times of homogeneous *n*-heptane/air mixtures computed using the skeletal and the reduced 18-step mechanism with experimental data from shock tube experiments by Ciezki and Adomeit [1] and measurements in rapid compression machines by Minetti et al. [2] is shown in Fig. 1. Computational ignition delay times have been determined from the simulation of a homogeneous reactor at constant volume. The ignition delay times are given in an Arrhenius diagram as a function of the inverse of the initial temperature T^0 for lean, stoichiometric, and rich mixtures at three different pressures. For the experiments, ignition is defined by the maximum CH band emission. In the calculations, the ignition criterion is at the highest temperature rate of change with respect to time, which coincides very well with the maximum CH concentration. Despite the very concise representation of the low-temperature kinetics, the agreement between calculated and measured data is very good, even at low pressures. No appreciable difference can be observed between the results from the skeletal and the reduced mechanism.

In addition to the ignition delay times, the delay of the first stage in multistage ignitions, τ_1, is given in Fig. 1 for different equivalence ratios, but only for the highest pressure. Also shown are the experimental data by Ciezki and Adomeit [1]. Since the temperature and pressure rise during the first stage of ignition are not very sharp, the calculated values of τ_1 are defined as the time of the first maximum of the OH concentration. The predicted values for τ_1 are too long, but, especially at low equivalence ratios, the agreement is still reasonable.

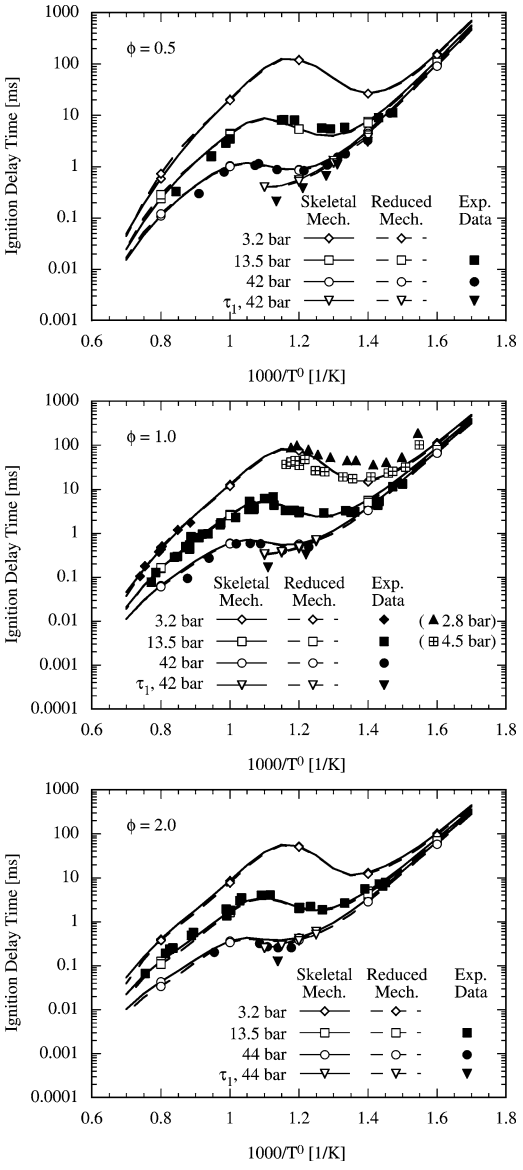

Fig. 1. Homogeneous ignition delay times of n-heptane/air mixtures for different pressures and equivalence ratios ϕ as a function of initial temperatures in a comparison of numerical simulations with experimental data from shock tube [1] and rapid compression machine (RCM) experiments [2]. The low pressure data at $\phi = 1$ is from the RCM experiments.

For a further validation of the mechanism, simulations have been performed for the plug flow reactor experiments by Held et al. [27], who studied n-heptane oxidation in highly diluted mixtures at 3 atm. The experiment is simulated as a homogeneous reactor at constant pressure. Two different conditions are considered here: a lean case at an equivalence ratio of $\phi = 0.79$ and an initial temperature of $T^0 = 940$ K and a rich case at $\phi = 2.27$ and $T^0 = 1075$ K. The

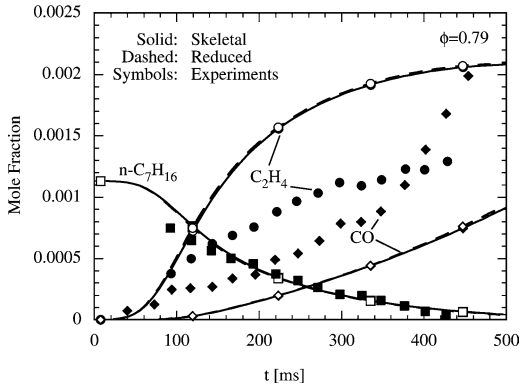

Fig. 2. Numerical results for lean n-heptane oxidation in a plug flow reactor compared with experimental data by Held et al. [27].

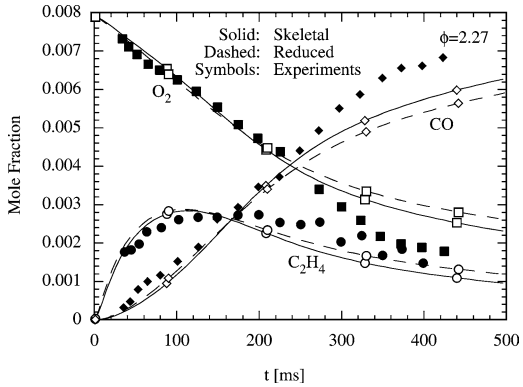

Fig. 3. Numerical results for rich n-heptane oxidation in a plug flow reactor compared with experimental data by Held et al. [27].

results of the simulations for the skeletal and the reduced mechanism are compared with the experimental data in Figs. 2 and 3. For the rich case, both mechanisms show excellent agreement where the conversion rate for the skeletal mechanism is only marginally higher than the 18-step mechanism. For the lean case, the induction period is represented quite accurately, but the predicted conversion of smaller intermediates to CO seems to be too slow.

Fig. 4 shows the temperature increase after a fixed reaction time of 1.8 s from the stoichiometric oxidation of n-heptane at different initial temperatures. Experimental data for this configuration at 12.5 atm have been provided by Callahan et al. [9]. The reduced 18-step mechanism reproduces the results from the skeletal mechanism very well. Both mechanisms agree well with the experimental data at higher temperatures, but underpredict the temperature increase for initial temperatures lower than 700 K. This is consistent with the overprediction of the ignition delay

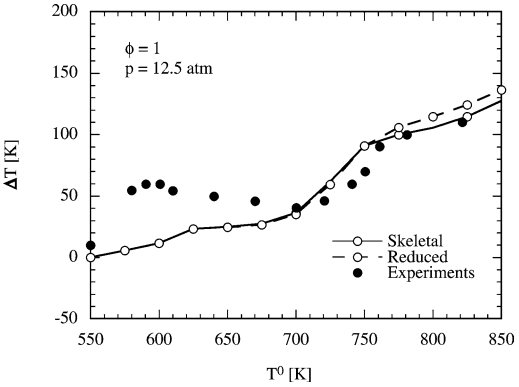

Fig. 4. Numerical results for temperature increase at a given time of reaction (1.8 s) of the stoichiometric n-heptane oxidation in a plug flow reactor compared with experimental data by Callahan et al. [9].

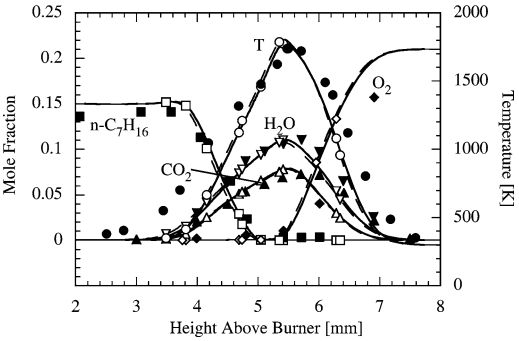

Fig. 5. Numerical results (solid lines with open symbols, skeletal mechanism; dashed lines with open symbols, reduced mechanism) of temperature and major species distribution in n-heptane/air counterflow diffusion flame compared with experimental data by Seiser et al. [28] (filled symbols).

time for the first stage of ignition in the shock tube calculations shown in Fig. 1.

Finally, the behavior of the mechanisms for steady flames is shown in Figs. 5 and 6. Results obtained from both mechanisms are compared with experimental data from an n-heptane counterflow diffusion flame by Seiser et al. [28]. The experiment has been performed at 1 atm for a strain rate of $a = 150\ \mathrm{s}^{-1}$. Other details of the configuration can be found in Seiser et al. [28]. The oxidizer is air and the fuel is diluted with nitrogen, such that the stoichiometric mixture fraction is $Z_{\mathrm{st}} = 0.1$. As suggested by Seiser et al. [28], to account for the effect of buoyancy, the profiles have been shifted by 0.34 mm away from the fuel duct. The results of the skeletal and the reduced 18-step mechanism agree well with each other. The predictions are also in very good agreement with the experimental data for temperature and the major species shown in Fig. 5. The comparison of mi-

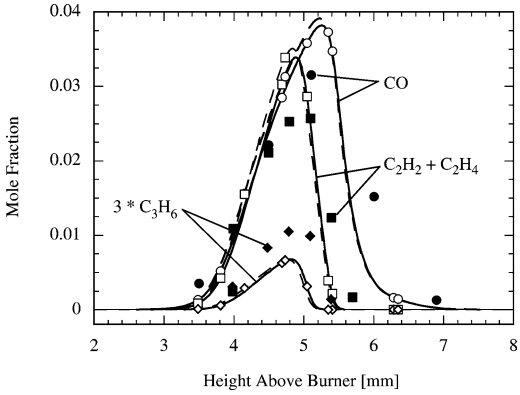

Fig. 6. Numerical results (solid lines with open symbols, skeletal mechanism; dashed lines with open symbols, reduced mechanism) of intermediate species distribution in n-heptane/air counterflow diffusion flame compared with experimental data by Seiser et al. [28] (filled symbols).

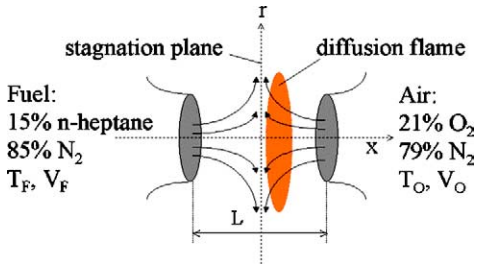

Fig. 7. Schematic of counterflow configuration.

nor species profiles with the experimental data shows some differences, but the agreement is still very good.

3. Overview of numerical simulation

The skeletal chemical kinetic mechanism for n-heptane ignition and oxidation described in the previous section is used to study the ignition process in inhomogeneous systems to identify critical rate-limiting elementary reaction steps. The reduced 18-step mechanism is not used in the present one-dimensional unsteady ignition study; however, relative to the skeletal mechanism, its efficiency may make it feasible to perform multidimensional simulations of n-heptane ignition processes. The present numerical configuration corresponds to a steady, axisymmetric, laminar flow of two impinging streams, issuing from two nozzles separated by a distance L, as schematically illustrated in Fig. 7. The main flow is in the axial direction, denoted by the coordinate x. At the left boundary ($x = 0$), the fuel stream flows from a nozzle at a temperature of T_F with a constant velocity normal to the stagnation plane, V_F. The fuel stream consists of prevaporized n-heptane maintained at a

mass fraction of Y_F ($Y_F = 0.38$ in the present study), with the remainder of the fuel stream being nitrogen. Air is supplied from the right boundary ($x = L$) at T_O and V_O. The velocities V_F and V_O are determined such that the momentum of the two streams is equal, and there is a stagnation plane close to the midpoint of the domain. Ignition simulations are performed at a constant pressure of 40 atm (except for consideration of pressure effects in Section 6) with a domain length of $L = 0.5$ cm. Boundary air and/or fuel temperatures are adjusted to affect the ignition kinetics. Simulations are conducted using OPUS [29]. Initial conditions are obtained in a two-step process: a fully burning OPPDIF [30] result is used to obtain a well-refined mesh, and this mesh is used to provide the OPUS initial condition by obtaining a new solution with all reaction terms suppressed so that only reactants are present. CHEMKIN software libraries [31] are interfaced with both OPUS and OPPDIF to evaluate reaction rates as well as thermodynamic and transport properties.

4. Multistage ignition phenomena

Ignition can be defined as the transition from relatively slow chemistry to the relatively fast chemistry typical of high-temperature combustion. The conditions under which ignition occurs in certain inhomogeneous systems is studied in this paper. At the most fundamental level, ignition occurs when the rates of heat release and/or chain-branching are fast relative to the various loss mechanisms [32]. The loss mechanisms of concern for the present inhomogeneous ignition conditions are diffusive transport of thermal energy, reaction intermediaries, and products from the reaction zone to surrounding less reactive gases. In hydrocarbon fuels, three types of ignition chemistry can be identified and losses can affect any of these.

At the lowest temperatures, a chain-branching process centered on the OH radical dominates ignition chemistry. The OH radical formed in this process rapidly abstracts a H atom from the fuel, *n*-heptane in the present study, through reactions R99 and R100, where the reaction number here refers to the reaction step in the skeletal mechanism given in Appendix A. The resulting alkyl radical reacts rapidly with molecular oxygen to form $C_7H_{15}O_2$ (R105f, R106f) and then isomerizes to form $C_7H_{14}OOH$ (R107). A subsequent O_2 addition (R108) is followed by another isomerization (R109) and release of one OH (R110). A typical product of this last isomerization is a keto-heptylperoxide (referred to henceforth as KET). Up to this point the process is chain-carrying, consuming the same number of radicals as it produces and releasing a moderate amount of heat (26.8 kJ per mole of fuel). The KET then decomposes (R111) to products including an additional OH radical, making the sequence chain-branching. The last decomposition step (R111) has relatively high activation energy and there tends to be a buildup of KET while the low-temperature chemistry occurs.

At temperatures near 900 K, although the exact temperature is pressure dependent, the chemical equilibrium for the addition of O_2 to heptyl radicals shifts strongly toward dissociation back to heptyl and O_2 (R105b, R106b). This greatly reduces the concentration of $C_7H_{15}O_2$ available for isomerization and for the low-temperature chain-branching process. At the same time, the rates for beta-scission reactions become significant (e.g., R85, R86, R88, R91, R92, R93), and the resulting smaller alkyls tend to react with O_2 to form HO_2 (R66f, R74f, R82f). The HO_2 reacts with itself to form H_2O_2 (R14), making the sequence essentially chain-terminating until the H_2O_2 dissociates to form a pair of OH (R15). This dissociation has high activation energy and only results in a chain-carrying sequence. Because of the slow rate of H_2O_2 dissociation and the slow rate of radical branching, this intermediate-temperature chemistry tends to progress more slowly toward ignition with a rate that increases strongly with increasing temperature. More detailed analysis of the relevant reaction kinetics can be found in Refs. [3] and [4].

At higher temperatures, the rate of the branching reaction $H + O_2 \rightarrow OH + O$ (R1) becomes faster than the chain-terminating reactions, typically $H + O_2 + M \rightarrow HO_2 + M$ (R8), and the overall rates of reaction increase rapidly due to branching. At these temperatures, the chemistry is significantly faster than that of either the low- or intermediate-temperature regimes.

For certain initial conditions, heat release associated with the low-temperature chemistry causes a transition in the kinetics from the low- to intermediate-temperature chemistry, resulting in what is referred to as two-stage ignition. The two-stage ignition chemistry typical of large hydrocarbons is a consequence of reduced reaction rates in the intermediate-temperature regime. For relatively low initial temperatures, at a time when the transition from low- to intermediate-temperature kinetics occurs, fuel has been totally consumed, and thus ignition progresses directly to high-temperature chemistry such that the ignition process is dominated by low-temperature kinetics. This is the so-called single-stage low-temperature chemistry dominated ignition. For relatively high initial temperatures, ignition bypasses the low-temperature chemistry and starts directly from the intermediate-temperature chemistry. This condition is referred to as single-stage intermediate-temperature chemistry dominated igni-

tion. More detailed information on multistage ignition for n-heptane in homogeneous systems can be found in Refs. [3] and [4].

Ignition is primarily dependent on the consumption of fuel by radicals, primarily OH, and thus radical production through branching reactions is critical. However, the key branching reactions have relatively large activation energies and are sensitive to heat losses from the reaction zone. These key reactions are the dissociation of KET (R111) in the low-temperature regime and H_2O_2 decomposition (R15) in the intermediate-temperature regime. Based on this understanding of ignition chemistry for homogeneous systems, heat and radical losses in inhomogeneous systems are the focus of the present study. The critical ignition phenomena are identified in the spatial dimension through local maxima of OH concentration in time; the location of these maxima is defined as the ignition kernel. The ignition delay, t_{ig}, similar to homogeneous systems defined in the previous section, is the time at the kernel when the temperature rate-of-change experiences a maximum, $(\partial^2 T/\partial t^2)_{t_{\mathrm{ig}}} = 0$, indicating a maximum in the heat release rate. For those conditions that exhibit a distinct two-stage ignition, the ignition delay associated with the first stage, τ_1, is defined as the time at which the maximum OH at the kernel is attained, $(\partial Y_{\mathrm{OH}}/\partial t)_{\tau_1} = 0$.

For the skeletal mechanism, the fraction of fuel consumed by low-temperature chemistry (through R107) is defined by

$$\alpha = \frac{\omega_{107}}{\sum_{i=97}^{104} \omega_i}, \tag{1}$$

where ω_i (mol/cm^3/s) is the reaction rate of reaction i. Because the interchange between heptyl and heptylperoxy (R105 and R106) is fast and reversible, it is the essentially irreversible reaction R107 that determines the moles of fuel that are consumed by the low-temperature branch. A value of $\alpha = 1$ indicates that all of the fuel is oxidized by the low-temperature chemistry, whereas a value of $\alpha = 0$ indicates that the fuel is consumed through intermediate- and high-temperature paths. The value of α depends primarily on temperature, pressure, and oxygen concentration. For a fixed pressure of 40 atm, the chemistry for stoichiometric mixtures shifts from low-temperature to intermediate- and high-temperature ignition chemistry between 792 and 1005 K, where $\alpha = 0.95$ and $\alpha = 0.1$, respectively, using the skeletal mechanism. Between these two temperatures, the ignition kinetics is either dominated by low-temperature chemistry ($\alpha > 0.5$ or $T < 901$ K) or by intermediate-temperature chemistry ($\alpha < 0.5$ or $T > 901$ K). The temperature at $\alpha = 0.5$ is defined as the crossover temperature (901 K at 40 atm) [6], indicating the transition from a low-temperature- to an intermediate-temperature-dominated kinetics regime. Assuming heptyl and heptylperoxy radicals are in steady state, and neglecting the difference between the primary and secondary heptyl, α is estimated to be

$$\alpha \approx \frac{1}{1 + \frac{(k_{91}+k_{92}+k_{93})(k_{105b}+k_{106b}+k_{107})}{k_{107}(k_{105f}+k_{106f})[\mathrm{O_2}]}}, \tag{2}$$

where k_i is the rate constant of reaction i which depends on temperature and/or pressure, and $[O_2]$ is the initial oxygen concentration (mol/cm^3) in the mixture. The value of α at 40 atm is presented in Fig. 8 evaluated using Eq. (2) as a function of temperature for three equivalence ratios (ϕ), ranging from 0.5 to 30.0. It is found that α is dependent primarily on temperature rather than equivalence ratio (oxygen concentration). So for nonpremixed systems, the change in temperature between fuel and oxidizer is a stronger determinant of α at any spatial location than the change in stoichiometry. The pressure dependency of α is discussed later. Peters et al. [6] provide further excellent discussion of α for homogeneous systems.

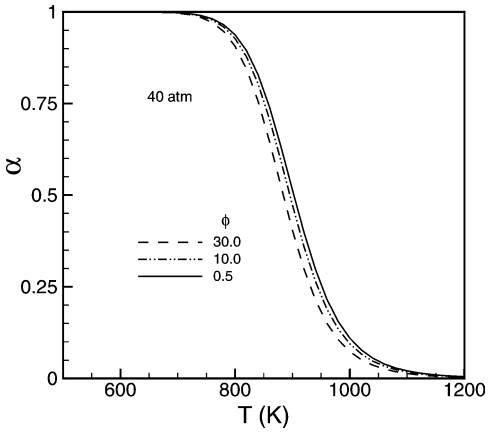

Fig. 8. The parameter α as a function of temperature at 40 atm for three equivalence ratios, ϕ, ranging from 0.5 to 30.0.

5. Results and discussion

The focus of the current paper is on ignition in mixtures where the fuel and the oxidizer are initially nonpremixed and on the effect of strain and temperature differences between the reactants on ignition. Two series of numerical experiments are conducted in physical space. In the first series the temperatures of the fuel and the oxidizer streams are equal, whereas in the second series the temperatures of the fuel and the oxidizer streams differ significantly. In all simulations the fuel stream is diluted with 85% nitrogen by

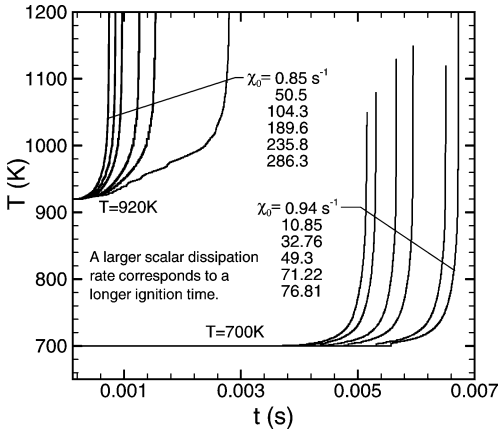

Fig. 9. Kernel temperature evolution during single-stage ignition for uniform boundary temperature ($T = 700$ K and $T = 920$ K).

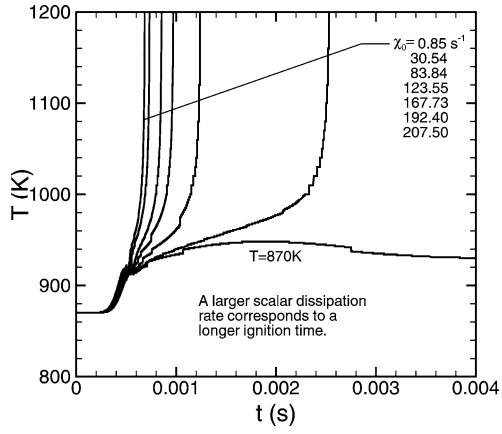

Fig. 10. Kernel temperature evolution during multistage ignition for uniform boundary temperature ($T = 870$ K).

volume ($Y_F = 0.38$) so that the stoichiometric point is shifted somewhat away from the oxidizer stream. In the counterflow configuration the velocity gradient imposes a diffusion rate or mixing rate, commonly referred to as the strain rate. To generalize this strain rate to other geometries, the scalar dissipation rate is used, which is measured in physical space, defined as

$$\chi = 2D(\partial\xi/\partial x)^2, \tag{3}$$

where, ξ is the mixture fraction [33] and D is the mixture thermal diffusivity.

5.1. Uniform boundary temperature

The first case to be considered corresponds to a uniform fuel and oxidizer boundary temperature of 700 K. For ignition in homogeneous systems at these low initial temperatures, the fuel is typically consumed in its entirety before the temperature increase bootstraps the mixture into the intermediate-temperature regime. Thus, ignition is a single-stage, low-temperature chemistry dominated process. For the nonpremixed reactants studied here, this is also true of the ignition kernel. Naturally, once ignition results in higher temperatures, the intermediate- and the high-temperature chemistries play important roles in the fuel consumption. As the scalar dissipation rate increases, the ignition delay is observed to rise as demonstrated by the kernel temperature evolution shown in Fig. 9, where χ_0 is the scalar dissipation rate evaluated at the stoichiometric location ($\xi = 0.146$) of the frozen flow. This scalar dissipation rate is the well-defined characteristic mixing rate for each simulation evaluated for frozen flow conditions. During the process of ignition, various chemical reactions take place at different stoichiometries; for example, low-temperature fuel chemistry tends to occur to the rich side of stoichiometry (except when the temperature gradients are strong enough to prevent reactions there). The local dissipation rate varies as a function of stoichiometry, primarily in accordance with the relationship derived in [34], and also as a function of increasing temperature in accordance with the temperature-dependent diffusion coefficient.

At somewhat higher temperatures, the heat release associated with the low-temperature ignition chemistry is sufficient to raise the temperature into the intermediate-temperature regime before all of the fuel is consumed. This is the case for a uniform boundary temperature of 870 K, where there is clear evidence of two-stage ignition, indicated in Fig. 10 by a temperature jump at the kernel during the ignition process. As before, increased scalar dissipation rate leads to an increase in the ignition delay and, if the scalar dissipation rate is sufficiently large, leads to inhibition of ignition ($\chi_0 = 207.5\ \text{s}^{-1}$ in Fig. 10). However, the effect of scalar dissipation rate on the low- and intermediate-temperature chemistry regimes is observed to be unequal. Specifically, strain primarily affects the intermediate-temperature chemistry in these two-stage ignition processes.

For higher boundary temperatures, e.g., at 920 K and above, the intermediate-temperature chemistry dominates, and the ignition process exhibits only a single-stage, as was observed for 700 K boundary temperatures. However, it differs in that the 920 K system is an intermediate-temperature chemistry dominated ignition. The kernel temperature evolution for the 920 K boundary temperature is also shown in Fig. 9.

Ignition delays for uniform boundary temperatures of 700, 870, and 920 K are shown in Fig. 11 as a function of inverse scalar dissipation rate evaluated at the stoichiometric location of the frozen flow. It is evident that increased scalar dissipation rates lead

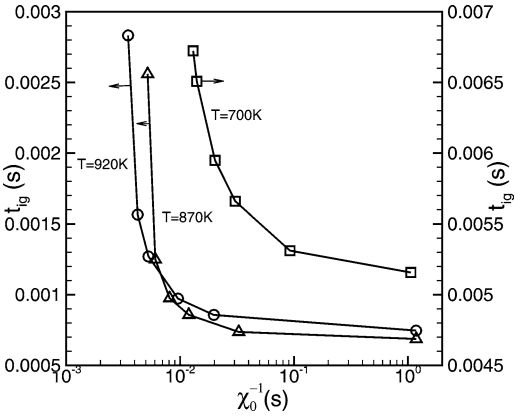

Fig. 11. Ignition delay as a function of inverse scalar dissipation rate for various uniform boundary temperatures.

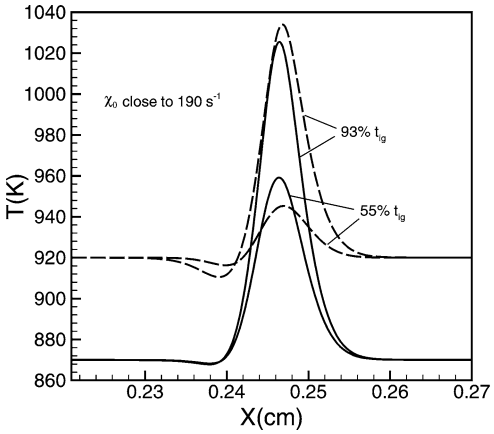

Fig. 12. Temperature profiles at 55 and 93% of ignition delay time for 870 K (solid) and 920 K (dashed), $\chi_0 \approx 190\ \mathrm{s}^{-1}$.

to longer ignition delay for all boundary temperatures, although this effect is only pronounced for large dissipation rates. The sensitivity of ignition delay to scalar dissipation rate can be explained by considering the conservation equation for a participant scalar variable such as temperature. In the conservation equation for a homogeneous system, there is a source term and a transient term that describe the rate of evolution of the system. In an inhomogeneous system like the present, there are additional dissipative terms that work against the source term and thus serve to reduce the rate of evolution toward ignition. If the dissipative term is sufficiently large, it balances the source term and the system's rate of evolution will be zero; this corresponds to a situation where ignition fails to occur (e.g., $T = 870$ K, $\chi_0 = 207.5\ \mathrm{s}^{-1}$ in Fig. 10). If the dissipative terms are small relative to the source term, the balance is between the transient evolution term and the source term and changes in dissipation have minimal effect on ignition delay as observed for small scalar dissipation rate in Fig. 11. This is in agreement with the asymptotic analysis for ignition in a stretched flow field [35].

As is shown in Fig. 11, for a boundary temperature of 700 K, the ignition delay is longer than for 870 and 920 K systems for the entire range of scalar dissipation rates studied here. This is due to the much slower low-temperature chemistry at 700 K compared with the low-temperature chemistry at 870 K, attributable to the large effective activation energy of the low-temperature chemistry. Comparing the cases with boundary temperatures of 870 and 920 K in Fig. 11, it is evident that, for low dissipation rates, the lower temperature system ignites earlier. This is an example of the negative temperature coefficient (NTC) behavior typical of fuels like *n*-heptane in homogeneous systems [4]. As observed in Fig. 10, for the system that started at 870 K, heat release associated with low-temperature chemistry causes the kernel temperature to rise to the vicinity of 920 K. Subsequently there is a delay associated with the intermediate-temperature chemistry. In the system initially at 920 K (Fig. 9), the intermediate-temperature chemistry dominates the entire ignition process. The kinetics associated with radical-pool buildup and fuel consumption are slow in the vicinity of 920 K compared to the low-temperature chemistry at 870 K leading to the NTC behavior. The difference between the two cases is that at the time the temperature increases to the vicinity of 920 K for the system beginning at 870 K, a radical-pool has accumulated and the fuel has been partially consumed such that the remainder of the ignition process proceeds more readily. Details can be found in studies of homogeneous systems [3,4].

It is also observed in Fig. 11 that, when dissipation significantly affects the ignition delay, the system at 870 K is more strongly affected, to the point that ignition is completely suppressed at lower scalar dissipation rates than for 920 K. This can be explained by considering the temperature gradients surrounding the kernel. Fig. 12 shows a comparison of the temperature profiles for boundary temperatures of 870 and 920 K, respectively, at early (55% of ignition delay) and late (93% of ignition delay) times for high scalar dissipation rate ($\chi_0 \approx 190\ \mathrm{s}^{-1}$). For systems where two-stage ignition is important, e.g., at 870 K, the second stage is most susceptible to dissipative heat losses (Fig. 10) because the associated temperature gradients are most severe. The difference between the single-stage, intermediate-temperature chemistry system (at 920 K) and the two-stage chemistry system (at 870 K) is the magnitude of the temperature gradient. For the two-stage chemistry the temperature gradient (dT/dx) at the earlier time (55% t_{ig}) is of the order 13500 K/cm, while for the single-

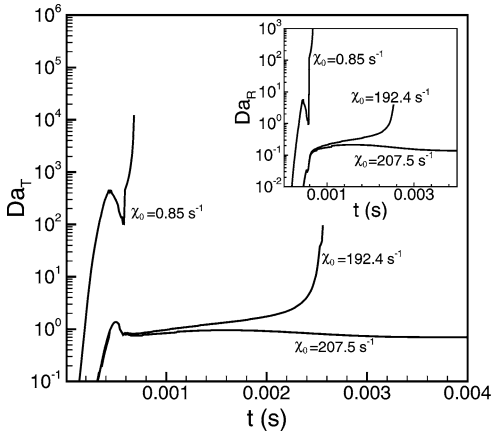

Fig. 13. Da_T at the kernel in the induction period for uniform boundary temperature of 870 K. (Inset) Da_R under the same conditions.

stage ignition the temperature gradient is of the order 4100 K/cm. Thus, more significant heat losses during the intermediate-temperature chemistry results in a slower temperature rise and a longer ignition delay for the lower boundary temperature of 870 K at a fixed scalar dissipation rate. This leads to the crossover observed in Fig. 11 at high dissipation rates.

The global effect of scalar dissipation rate may be represented by a Damköhler number (Da_T) based on the heat-release rate at the kernel, which is defined as

$$Da_T = \frac{(q/Y_F)/H_0}{\chi}, \tag{4}$$

where q (kJ/mol/s) is the instantaneous heat-release rate at the kernel, H_0 is the heat of combustion of n-heptane ($H_0 = 271$ kJ/mol n-heptane), Y_F, as mentioned earlier, is the mass fraction of fuel at the fuel stream ($Y_F = 0.38$), and χ is the instantaneous scalar dissipation rate evaluated at the kernel. The Damköhler number based on heat release, as presented in Fig. 13, is tracked through the induction period for three different scalar dissipation rates at a boundary temperature of 870 K. Da_T increases significantly during the first stage, low-temperature chemistry. Following the transition from low- to intermediate-temperature kinetics the Damköhler number decreases for a short time, reflecting the intermediate-temperature chemistry susceptibility to dissipative heat losses. Reaction flux analysis indicates that the rate-limiting reaction in the intermediate-temperature chemistry is the H_2O_2 dissociation reaction, R15. The decrease of Da_T occurs in conjunction with this slow reaction becoming the dominant chain-branching reaction at early times of the second stage. For conditions where ignition occurs, the value of Da_T is significantly greater than unity at the time of ignition, indicating that the generation of heat occurs at a rate that is fast relative to dissipation of thermal energy. On the other hand, there also exist values of scalar dissipation rate (e.g., $\chi_0 = 207.5\ \mathrm{s}^{-1}$) that are sufficiently large so as to prevent ignition due to excessive heat loss relative to its generation. For these conditions, the transition to high-temperature kinetics and thermal runaway does not occur. The transition from igniting to nonigniting conditions corresponds to the lower turning point of the well-known "S" shape curve, indicating that although a steady-state flame solution can exist, nonignition is a stable solution above the critical scalar dissipation rate.

Similarly, the Damköhler number (Da_R) based on the H_2O_2 dissociation reaction, R15, is presented in the inset in Fig. 13, defined as

$$Da_R = \frac{(\omega W)/(\rho Y_F)}{\chi}, \tag{5}$$

where ω (mol/cm^3/s) is the consumption rate of H_2O_2 through R15 to produce a pair of OH radicals, W is the molecular weight of H_2O_2, and ρ is the density of the fuel stream. Interestingly, Da_R behaves qualitatively similar to Da_T, indicating that a single rate-controlling process affects both radical growth and heat release.

In summary, for uniform boundary temperature, ignition is inhibited when a large scalar dissipation rate leads to sufficient heat or radical loss to break the chain-branching behavior. Moreover, under high-strain conditions for two-stage ignition, it is found that ignition is inhibited during the second, intermediate-temperature stage where the dissociation of hydrogen peroxide is rate-limiting; self-generated temperature gradients resulting from multistage ignition are more severe, leading to dissipative losses larger than those for single-stage ignition.

5.2. Nonuniform boundary temperature

Temperature gradients between the fuel and oxidizer streams are typical in practical systems where the fuel stream is often cooler than the air stream because of smaller ratios of specific heats and enthalpy required to vaporize liquid fuels. The existence of a temperature gradient between the fuel and the oxidizer streams will be shown to have an additional inhibiting effect beyond that of scalar dissipation with uniform boundary temperatures. To demonstrate this, numerical simulations are conducted with fuel and oxidizer stream temperatures of 572 and 827 K, respectively. This fuel temperature corresponds to the boiling point of n-heptane at 40 atm and the oxidizer temperature is obtained by adiabatically compressing ambient air (300 K) from 1 to 40 atm. With these boundary temperatures, the entire domain evolves initially through low-temperature kinetics with the

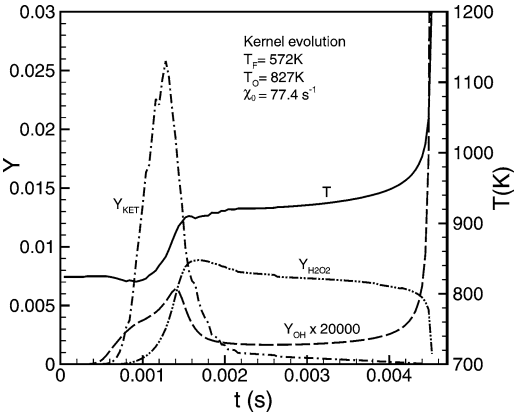

Fig. 14. Kernel evolution in the induction period for nonuniform boundary temperature ($T_F = 572$ K, $T_O = 827$ K, $\chi_0 = 77.4$ s^{-1}).

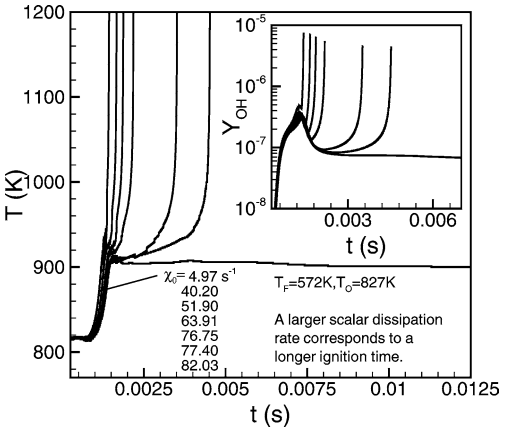

Fig. 15. Kernel temperature evolution in the induction period for nonuniform boundary temperature ($T_F = 572$ K, $T_O = 827$ K). (Inset) Y_{OH} evolution under the same conditions.

strongest reaction rates (the ignition kernel) occurring on the hot oxidizer side of the domain. As the OH concentration rises during the low-temperature kinetics, the kernel moves toward stoichiometric and then rich mixtures. The kernel region subsequently transitions to intermediate-temperature kinetics, at 1.4 ms (τ_1) with $\chi_0 = 77.4$ s^{-1} as shown in Fig. 14, demarcated by a temperature jump, the transition from KET to H_2O_2 as the intermediate of significance, and the appearance of a local OH maximum.

Similar two-stage ignition behavior is found for various scalar dissipation rates for these fuel and oxidizer temperatures. The kernel temperature evolution in the induction period for various scalar dissipation rates is presented in Fig. 15 and the inset shows Y_{OH} evolution at the kernel. Similar to the uniform boundary temperature case exhibiting two-stage ignition ($T = 870$ K), the effect of the scalar dissipation rate on ignition manifests itself mainly in the second stage where intermediate-temperature chemistry dominates. For low scalar dissipation rates, e.g., $\chi_0 = 4.96$ s^{-1}, ignition evolves like a homogeneous system, whereas for high scalar dissipation rates the delay occurs in the second stage. For scalar dissipation rates higher than a critical value above which ignition cannot occur, e.g., $\chi_0 = 82.03$ s^{-1}, ignition fails in the second stage, again indicating the slow reactions in the intermediate-temperature chemistry with relatively high heat and radical losses. For the particular temperatures shown here, ignition occurs for equivalence ratios near unity at low scalar dissipation rates and for equivalence ratios above 2 at high scalar dissipation rates [18].

To verify the effect of the scalar dissipation rate on the intermediate-temperature chemistry and to determine the rate-limiting reaction in this chemistry regime, a reaction flux analysis is performed for OH generation and destruction reactions for two different scalar dissipation rates, $\chi_0 = 40.2$ s^{-1} and $\chi_0 = 82.03$ s^{-1}, with the second representing failed ignition at the second stage. As is shown in Figs. 16 and 17 in both physical and mixture fraction coordinates, the dominant reactions are R15, R110, and R111 for OH generation and R36 and R100 for destruction. Late in the first-stage ignition where low-temperature chemistry still dominates (Fig. 16), reaction rates of R110, R111, R36, and R100 for low scalar dissipation rate are comparable with that for high scalar dissipation rate, indicating the negligible effect of scalar dissipation rate on low-temperature chemistry. Although Fig. 16 shows that the reaction rate of R15 is affected significantly by the scalar dissipation rate, other ignition reactions (R111 and R110) are more important during the first stage. Upon the transition from the first to the second ignition stage, low-temperature chemistry becomes less important than intermediate-temperature chemistry. This is the situation depicted in Fig. 17 where R15 is clearly the dominant reaction responsible for OH generation. For the smaller scalar dissipation rate, R15 and temperature increase gradually, whereas for the larger scalar dissipation rate the increase in R15 and temperature is negligible due to significant heat and radical losses at the kernel relative to heat and radical generation. Thus, scalar dissipation rate has an effect on intermediate-temperature chemistry much more profound than that on low-temperature chemistry for two-stage ignition. It is noteworthy that the peaks of the reactions for low and high scalar dissipation rates differ in physical location due to the strain effect, shown in Figs. 16a and 17a; however, they are solely determined by the temperature and composition (mixture fraction), as shown in Figs. 16b

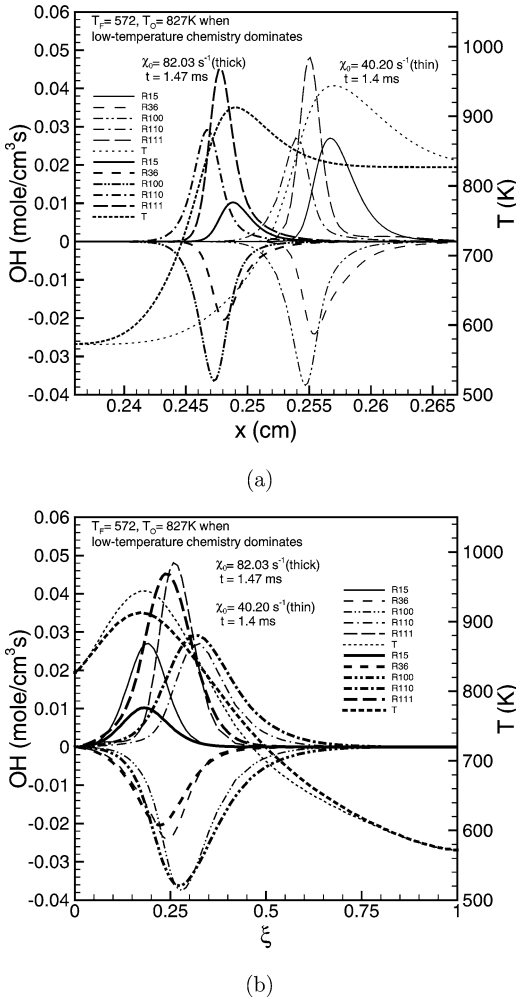

Fig. 16. OH reaction profiles for $\chi_0 = 40.20\ \mathrm{s}^{-1}$ and $\chi_0 = 82.03\ \mathrm{s}^{-1}$ with $T_F = 572$ K, $T_O = 827$ K late in the first-stage ignition (1.4 ms for $\chi_0 = 40.20\ \mathrm{s}^{-1}$ and 1.47 ms for $\chi_0 = 82.03\ \mathrm{s}^{-1}$) (a) in physical coordinates and (b) in mixture fraction coordinates where low-temperature chemistry dominates.

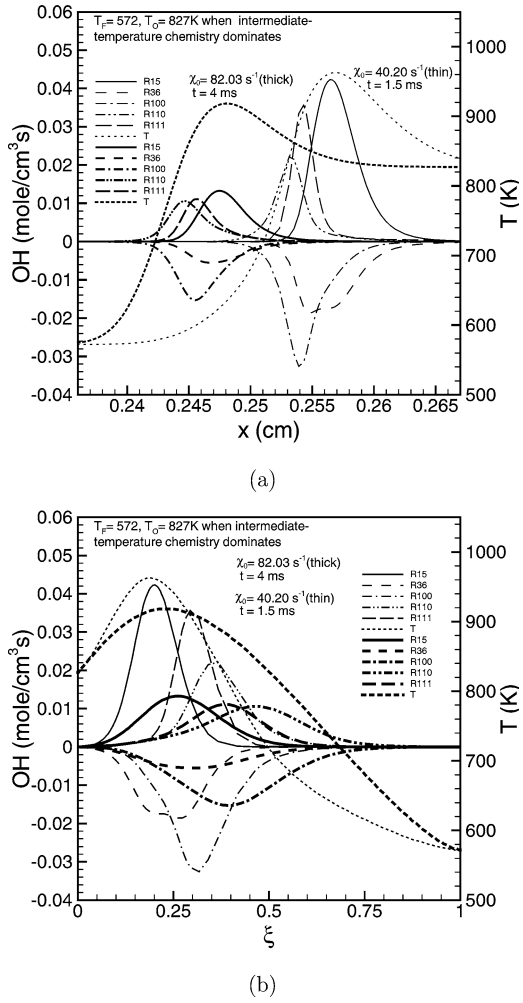

Fig. 17. OH reaction profiles for $\chi_0 = 40.20\ \mathrm{s}^{-1}$ and $\chi_0 = 82.03\ \mathrm{s}^{-1}$ with $T_F = 572$ K, $T_O = 827$ K during the second-stage ignition (1.5 ms for $\chi_0 = 40.20\ \mathrm{s}^{-1}$ and 4.0 ms for $\chi_0 = 82.03\ \mathrm{s}^{-1}$) (a) in physical coordinates and (b) in mixture fraction coordinates where intermediate-temperature chemistry dominates.

and 17b, which are independent of physical location.

The dependence of the ignition delay on the scalar dissipation rate (again evaluated at the stoichiometric position for the frozen flow) for these nonuniform boundary temperatures is shown in Fig. 18, contrasted with ignition delay for uniform boundary temperatures of 820 and 757 K. The uniform temperature of 820 K matches the temperature at the initial kernel location for the nonuniform temperature case, whereas 757 K matches the ignition delay for the nonuniform temperature case at low scalar dissipation rates. The following observations can be made from a comparison of these cases in Fig. 18: (1) nonuniform boundary temperature results in a longer ignition delay for high scalar dissipation rates; (2) the critical scalar dissipation rate is smaller for the nonuniform temperature case; and (3) comparable critical scalar dissipation rates are observed for two uniform temperature cases, though the boundary temperature differs, because of the varying roles of low- and intermediate-temperature chemistry as is described shortly.

First, consider the difference between the uniform boundary temperature of 820 K and the nonuniform boundary temperatures. By tracking the kernel evolution or from the analysis of the relationship between α and temperature described in an earlier section, it is known that a uniform temperature of 820 K also ex-

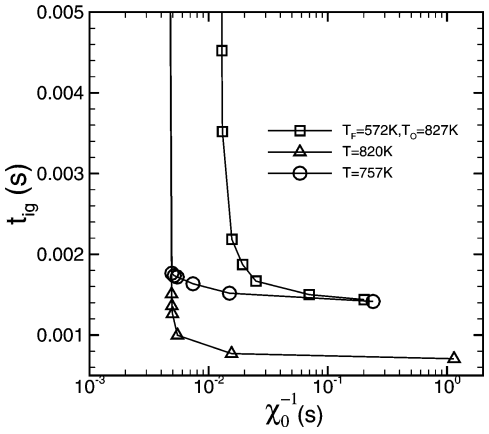

Fig. 18. Ignition delay versus the inverse of scalar dissipation rate for nonuniform boundary temperatures of $T_F = 572$ K and $T_O = 827$ K compared with uniform boundary temperatures, $T = 820$ K and $T = 757$ K.

hibits two-stage ignition. For both cases, the temperature gradient associated with the transition from the first to the second stage of ignition reduces the width of the kernel (reaction zone), thereby increasing dissipative losses. This is demonstrated in Fig. 19, which presents the temperature and mass fraction profiles for a scalar dissipation rate close to 64 s^{-1} at times when the kernel temperature rise is approximately 120 K for the nonuniform (at 1.83 ms) and uniform (at 0.71 ms) boundary temperature cases. This particular temperature rise brings the ignition kernel to temperatures where it is dominated by intermediate-temperature kinetics and where the ignition kernel is most susceptible to strain. The initial temperature and OH mass fraction for the nonuniform temperature case is also shown in Fig. 19a for reference. The reaction-zone thickness, defined as the full width at half maximum of the OH profiles, shown in Fig. 19a, is 49 and 88 μm for nonuniform and uniform cases, respectively. Differences observed in width are due to the added effect of the imposed temperature gradient for the nonuniform case. Moreover, the branching reactions R111 and R15 have relatively large activation energies and, hence, are rapidly reduced as the colder fuel stream is approached for the nonuniform case.

The effect of temperature gradient on ignition delay has long been known for simplified chemistry [12,13] and it is interesting that the same result seems applicable to multistage chemistry. It is noteworthy that, for this particular (typical) range of temperatures, both the low- and intermediate-temperature chemistries are active throughout the domain, and both are narrowed by the temperature gradient, as demonstrated in Fig. 19b. Low-temperature chemistry is represented by KET and intermediate-temperature chemistry by H_2O_2 since the branching of these in-

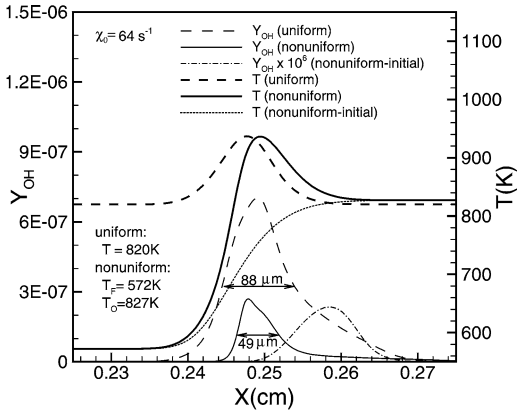

(a)

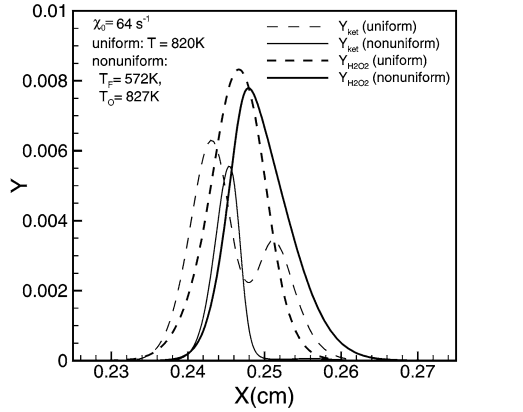

(b)

Fig. 19. Profiles of (a) temperature and Y_{OH} and (b) $Y_{H_2O_2}$ and Y_{ket} for nonuniform boundary temperatures of $T_F = 572$ K and $T_O = 827$ K (solid) at 1.83 ms compared with uniform boundary temperature of $T = 820$ K (dashed) at 0.71 ms when kernel temperatures have risen approximately 120 K. The initial temperature and Y_{OH} profiles are also shown in (a) for the nonuniform boundary temperature case.

termediates produces OH. The twin peaks of KET are due to the higher generation rate of KET at certain temperatures and compositions. The minimum KET between the two peaks is due to the higher consumption rate of KET at the relatively higher temperature locally. The coexistence of both low- and intermediate-temperature chemistry in this particular temperature range enhances ignition by generating heat and radicals through both chemistries.

In addition to a comparison of uniform and nonuniform boundary temperatures that both exhibit two-stage ignition, consider the comparison between the nonuniform temperature case and a uniform boundary temperature of 757 K. This uniform boundary temperature is representative of single-stage low-

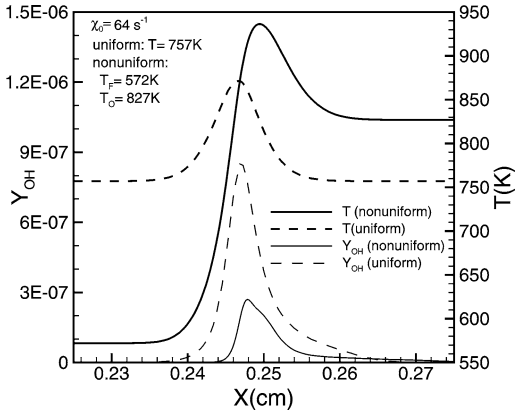

Fig. 20. Profiles of temperature and Y_{OH} when kernel temperatures have risen 120 K for nonuniform boundary temperatures of $T_F = 572$ K and $T_O = 827$ K (solid) at 1.83 ms compared with uniform boundary temperature of $T = 757$ K (dashed) at 1.47 ms.

temperature chemistry dominated ignition, similar to the 700 K case discussed in the previous section. The temperature of 757 K is selected because the low-strain rate ignition times are the same as those for the nonuniform temperature case (Fig. 18), indicating similar kinetic time scales when the kinetics are not influenced by mixing. Fig. 20, similar to Fig. 19, shows the profiles of the temperature and Y_{OH} for this comparison when the kernel temperature increase is approximately 120 K at 1.83 and 1.47 ms for nonuniform and uniform boundary temperatures, respectively. It also shows the effect of temperature gradient on further decreasing the reaction-zone thickness and increasing dissipative losses for the nonuniform temperature case. Interestingly, the kernel temperature for the uniform case (870 K) is lower than that for the nonuniform case (940 K); however, the maximum value of OH for the uniform case is much higher than that for the nonuniform case. This occurs because the low-temperature chemistry is much faster than the intermediate-temperature chemistry at their respective kernel temperatures. However, it takes a much longer time for the kernel temperature to increase 120 K at a uniform boundary temperature of 757 K (1.47 ms) due to the slow chemistry compared to the 820 K system (0.71 ms) which starts at a relatively higher temperature in the low-temperature kinetics regime.

Finally, a smaller critical scalar dissipation rate for nonuniform conditions is expected due to the additional effect of the imposed temperature gradient. However, for uniform conditions for two different boundary temperatures of 757 and 820 K, a comparable critical scalar dissipation rate is observed. The similar value of the critical scalar dissipation rate simply indicates that the rate-limiting reactions for both systems are comparable; i.e., that the rate of R111 in the 757 K system is comparable with the rate of R15 in the 820 K system when both reaction zones are subject to high dissipation rates. This expands on the earlier conclusion that for two-stage ignition the low-temperature chemistry is faster than the intermediate-temperature chemistry by noting that, for some lower temperature, the low-temperature kinetics are comparable to the intermediate-temperature kinetics. At high dissipation rates, the comparable kinetics occur for a temperature pair that differs from that temperature pair for which the kinetics are comparable at low dissipation rates or for homogeneous systems.

The global effects of scalar dissipation rate on ignition for nonuniform boundary temperature can also be represented by the Damköhler numbers, Da_T and Da_R. The trends observed for Da_T and Da_R are qualitatively similar to those observed for uniform boundary temperature cases and, hence, are not discussed in further detail.

In summary, for nonuniform boundary temperature, ignition is further delayed by the imposition of temperature gradients because the reaction zones for both low- and intermediate-temperature chemistries are narrowed beyond that for similarly strained uniform boundary temperature conditions. This leads to a smaller critical scalar dissipation rate compared to uniform boundary conditions. Similar to uniform boundary temperature cases, ignition in the second stage for two-stage ignition is found to be more susceptible to dissipative losses. This is attributed to the slow rate-limiting chemistry and the self-generated temperature gradient associated with the transition from low- to intermediate-temperature chemistry.

5.3. *Effect of fuel temperature on ignition*

Diesel fuel evaporates over a range of temperatures that depends on the fuel constituents. Typically *n*-heptane is at the low end of this temperature range. To understand the effect of the fuel-distillation temperatures on ignition, a series of fuel temperatures (572, 604, 762, and 920 K) was considered, with the oxidizer temperature fixed at 920 K. Due to the higher oxidizer temperature relative to the fuel temperature, the kernel is located closer to the oxidizer stream initially ($\phi \approx 0.03$), and thus the initial kernel temperature is nearly constant over the range of fuel stream temperatures selected. In time, the kernel migrates to a location where the chemistry (both low- and intermediate-temperature chemistry) is fast. There are two potential outcomes of varying the fuel stream temperature: (1) a lower fuel stream temperature leads to a higher temperature gradient, thereby reducing the chemical rates as the fuel stream is approached; or (2) a higher fuel temperature may bypass

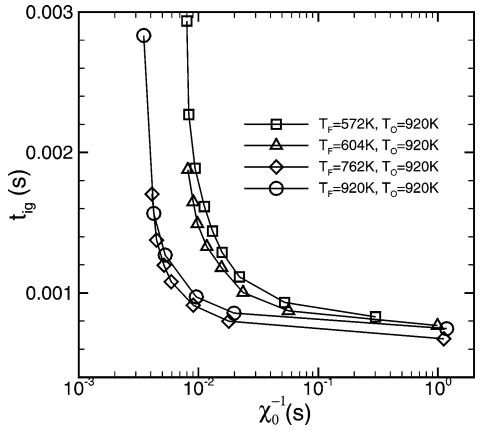

Fig. 21. Ignition delay versus the inverse of scalar dissipation rate for various fuel boundary temperatures, with oxidizer temperature fixed at $T_O = 920$ K.

the low-temperature chemistry and result in a single-stage intermediate-temperature chemistry dominated ignition, which may be slower than two-stage ignition. The two mechanisms compete leading to distinct ignition behavior, as shown in Fig. 21, from the correlations of ignition delay with scalar dissipation rate evaluated at the stoichiometric location of the frozen flow.

First, Fig. 21 shows that lower fuel-stream temperatures lead to a longer ignition delay for fuel temperatures of 572, 604, and 762 K. Ignition occurs more rapidly as the temperature gradient is reduced, but where the kernel is still dominated by low-temperature chemistry (i.e., α nearly unity). Therefore, of the three cases considered, ignition occurs the fastest for a fuel temperature of 762 K. Consistent with this, the critical scalar dissipation rate is also higher for the higher fuel boundary temperature, shown in Fig. 21.

Second, for a fuel boundary temperature of 920 K, the chemistry is entirely in the intermediate-temperature regime. Comparing the curves for 762 and 920 K in Fig. 21, for the lower fuel-boundary temperature ignition delay is shorter at low scalar dissipation rate and longer or comparable at high scalar dissipation rate. The argument for this behavior is the same as for the uniform boundary temperature cases, 870 and 920 K, described in Section 5.1, where the NTC behavior is present for low scalar dissipation rates, similar to a homogeneous system. For high scalar dissipation rates, the loss of heat and radicals for the second stage of the two-stage ignition in the 762 K system is more severe than that for the 920 K system because of the additional temperature gradient created by the temperature jump associated with the transition from low- to intermediate-temperature chemistry for the 762 K systems.

In summary, increasing the fuel-stream temperature reduces ignition delays as long as the initial chemistry occurs in the low-temperature regime. When the fuel temperature rises sufficiently that the chemistry is occurring in the NTC regime, this behavior may be reversed. At high dissipation rates, though, the NTC behavior is less evident because of the previously described significance of second-stage heat losses. Since practical ignition processes occur at high scalar dissipation rates, it is suggested that, for a fixed oxidizer temperature, e.g., 920 K at 40 atm, faster ignition is obtained if the temperature of the fuel stream is maximized, but still within the temperature range where α (Eq. (2)) is close to unity.

6. Effect of pressure on ignition

In practical diesel engine ignition conditions pressure is usually higher than 40 atm. The results from the current study may still be applicable by considering the effect of pressure on ignition chemistry. The pressure scaling for homogeneous systems is largely valid for inhomogeneous systems provided that it is applied to the vicinity of the kernel. The scaling includes the shift of the crossover temperature that determines the dominant chemistry to a higher temperature as pressure increases. The analysis of the parameter α, as functions of temperature, pressure, and oxygen concentration in the present study, differs with that of Peters et al. [6] in that the species steady-state assumptions and chemical mechanism are different. The dependence of the parameter α on temperature and pressure is presented in Fig. 22 for a stoichiometric n-heptane/air mixture.

It is seen from Fig. 22 that the crossover temperatures are 901 and 950 K at pressures of 40 and

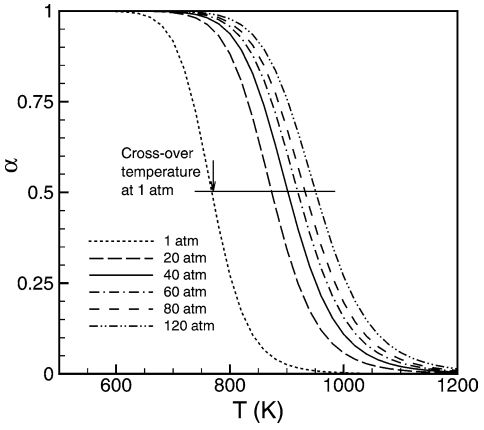

Fig. 22. The parameter α representing the fraction of heptyl radicals oxidized by the low-temperature chain for various pressures ($\phi = 1$).

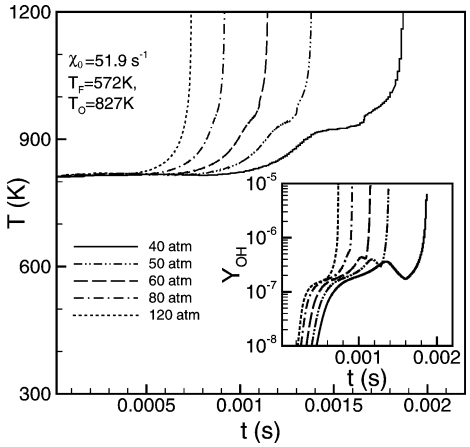

Fig. 23. Kernel temperature and Y_{OH} (inset) evolution for a nonuniform boundary temperature condition ($T_F = 572$ K, $T_O = 827$ K, $\chi_0 = 51.9\ s^{-1}$) at various pressures.

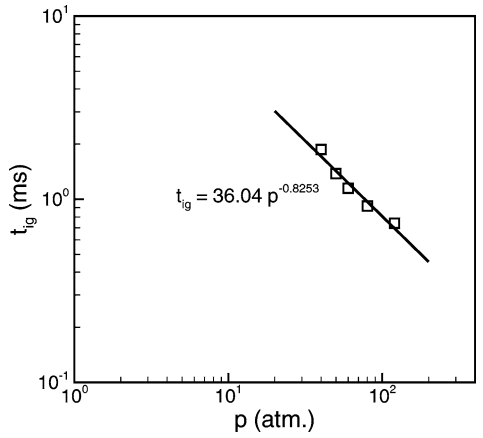

Fig. 24. Ignition delay time as a function of pressure for a nonuniform boundary temperature condition ($T_F = 572$ K, $T_O = 827$ K, $\chi_0 = 51.9\ s^{-1}$).

120 atm, respectively, which represents 50 K increase in temperature. This implies that, for the current fuel and oxidizer temperature for the uniform as well as the nonuniform boundary temperatures, two-stage ignition may revert to a single-stage low-temperature chemistry dominated ignition. Due to an increase in pressure, the reaction rates increase accordingly and thus accelerate the ignition process. This is demonstrated in Fig. 23 for the case of fuel and oxidizer boundary temperatures of 572 and 827 K and a scalar dissipation rate of approximately $\chi_0 = 52\ s^{-1}$ at different pressures. The scalar dissipation rate, evaluated at the stoichiometric location for the frozen flow, over the range of pressures remains nearly constant as a result of the competitive effects of decreasing thermal diffusivity and increasing mixture fraction gradient as pressure increases.

Fig. 23 shows that the ignition delay is reduced with an increase in pressure. For higher pressure, e.g., 120 atm, ignition is low-temperature chemistry dominated single-stage ignition, which is slower than two-stage ignition for the same pressure. However, the ignition time is much less than that for two-stage ignition at lower pressures, e.g., 40 atm. This indicates that the increase in reaction rates due to an increase in pressure is much more significant than the shift in crossover temperature which determines the transition of single-stage ignition to two-stage ignition. Thus, an increase in pressure will decrease the ignition delay considerably. The pressure dependence of the ignition delay time shown in Fig. 23 can be fitted to a power relationship, $t_{ig} = 36.04p^{-0.8253}$, shown in Fig. 24. The observed dependence is consistent with the analytical solution obtained for a homogeneous mixture shown in Fig. 13 of Ref. [6]. A decrease in ignition delay with increasing pressure was also observed in a diesel-spray ignition experiment where fuel was injected into an ambient gas representing air at a temperature of 1000 K, density of 14.8 and 30.0 kg/m^3, corresponding to pressures of 41 and 84 atm, respectively, in Fig. 11 [36]. The effect of strain-induced gradient and imposed temperature gradient for uniform and nonuniform boundary temperature conditions on ignition remains valid for high pressures.

7. Conclusion

The effect of steady strain on the transient autoignition of *n*-heptane at high pressures in a counterflow configuration is studied numerically with detailed chemistry and transport. Newly developed skeletal and reduced *n*-heptane mechanisms are validated over a range of pressures and stoichiometries. Transient ignition simulations with uniform and nonuniform boundary fuel and oxidizer temperatures are performed using the skeletal mechanism so that the critical rate-limiting elementary reaction steps in the ignition process can be identified.

For both configurations at low scalar dissipation rates, ignition exhibits behavior similar to that found for homogeneous systems, including the negative temperature coefficient (NTC) regime. However, this behavior changes when scalar dissipation rates are increased to a point where losses of radicals and heat are significant. Strain-induced gradients delay ignition because they reduce the reaction-zone thickness and increase losses of heat and radicals produced during the ignition process. These losses are more significant for two-stage ignition than for single-stage ignition because the temperature rise associated with the transition from low- to intermediate-temperature chemistry results in more severe temperature gradients. The

second, intermediate-temperature stage is found to be more sensitive to strain/dissipation than the first low-temperature stage in two-stage ignition. When the fuel and oxidizer boundary temperatures are nonuniform, ignition is further delayed because the reaction zone is narrowed beyond that for similarly strained ignition with uniform boundary temperatures. This is true of both the low- and intermediate-temperature chemistries, which can coexist at different positions across the physical domain for the appropriate conditions.

The global effects of the scalar dissipation rate are presented in terms of a Damköhler number based on the heat-release rate or characteristic chain-branching rate, normalized by the characteristic diffusion rate at the kernel. Ignition occurs when the Damköhler number of the system is well above a critical value, representing the balance between heat or radical generation and the losses of heat or radicals due to strain-induced and/or temperature stratification-induced gradients.

Results suggest that, to minimize ignition delay for nonuniform boundary temperatures, the fuel temperature should be adjusted to as high a temperature as possible while maintaining the parameter α close to unity. In this manner, for turbulent environments characterized by high scalar dissipation rates, the ignition delay can be shortened by proceeding through two-stage ignition, rather than through intermediate-temperature chemistry dominated ignition. This presumes that the oxidizer temperature is not sufficiently high such that the intermediate-temperature chemistry is fast.

Pressure effects on ignition are comparable to those of homogeneous systems. The crossover temperature increases with pressure, and hence, for a given boundary temperature, a two-stage ignition shifts to a single-stage low-temperature chemistry dominated ignition. However, the increase in reaction rate with pressure is more significant than the shift in the dominant chemistry. Hence, ignition delay is reduced with increasing pressure.

Acknowledgment

This research was supported by the Division of Chemical Sciences, Geosciences, and Biosciences, Office of Basic Energy Sciences, U.S. Department of Energy.

Appendix A
Skeletal mechanism for *n*-heptane

Number	Reaction	*A*	*n*	*E*
1f	$O_2 + H \rightarrow OH + O$	2.000E+14	0.00	70.3
2f	$H_2 + O \rightarrow OH + H$	5.060E+04	2.67	26.3
3f	$H_2 + OH \rightarrow H_2O + H$	1.000E+08	1.60	13.8
4f	$2OH \rightarrow H_2O + O$	1.500E+09	1.14	0.42
5f	$2H + M' \rightarrow H_2 + M'$	1.800E+18	−1.00	0
6f	$2O + M' \rightarrow O_2 + M'$	2.900E+17	−1.00	0
7f	$H + OH + M' \rightarrow H_2O + M'$	2.200E+22	−2.00	0
8f	$H + O_2 + M' \rightarrow HO_2 + M'$	2.300E+18	−0.80	0
9f	$HO_2 + H \rightarrow 2OH$	1.500E+14	0.00	4.2
10f	$HO_2 + H \rightarrow H_2 + O_2$	2.500E+13	0.00	2.9
11f	$HO_2 + H \rightarrow H_2O + O$	3.000E+13	0.00	7.2
12f	$HO_2 + O \rightarrow OH + O_2$	1.800E+13	0.00	−1.7
13f	$HO_2 + OH \rightarrow H_2O + O_2$	6.000E+13	0.00	0
14f	$2HO_2 \rightarrow H_2O_2 + O_2$	2.500E+11	0.00	−5.2
15f	$2OH + M' \rightarrow H_2O_2 + M'$	3.250E+22	−2.00	0
16f	$H_2O_2 + OH \rightarrow H_2O + HO_2$	5.400E+12	0.00	4.2
17f	$CO + OH \rightarrow CO_2 + H$	6.000E+06	1.50	−3.1
18f	$CO + HO_2 \rightarrow CO_2 + OH$	1.500E+14	0.00	98.7
19f	$CO + O + M' \rightarrow CO_2 + M'$	7.100E+13	0.00	−19
20	$CH + O_2 \rightarrow HCO + O$	6.000E+13	0.00	0
21	$CH + CO_2 \rightarrow HCO + CO$	3.400E+12	0.00	2.9
22f	$CH + H_2O \rightarrow CH_2OH$	5.700E+12	0.00	−3.2
23f	$HCO + M' \rightarrow CO + H + M'$	1.566E+14	0.00	65.9
24f	$HCO + O_2 \rightarrow CO + HO_2$	3.000E+12	0.00	0
25f	$3\text{-}CH_2 + H \rightarrow CH + H_2$	6.000E+12	0.00	−7.5
26f	$2\,3\text{-}CH_2 \rightarrow C_2H_2 + H_2$	1.200E+13	0.00	3.4
27f	$3\text{-}CH_2 + CH_3 \rightarrow C_2H_4 + H$	4.200E+13	0.00	0
28f	$3\text{-}CH_2 + O_2 \rightarrow CO + OH + H$	1.300E+13	0.00	6.2
29f	$3\text{-}CH_2 + O_2 \rightarrow CO_2 + H_2$	1.200E+13	0.00	6.2

(*continued on next page*)

Appendix A (*Continued*)

Number	Reaction	A	n	E
30f	$1\text{-}CH_2 + M' \rightarrow 3\text{-}CH_2 + M'$	1.200E+13	0.00	0
31f	$1\text{-}CH_2 + O_2 \rightarrow CO + OH + H$	3.100E+13	0.00	0
32f	$1\text{-}CH_2 + H_2 \rightarrow CH_3 + H$	7.200E+13	0.00	0
33f	$CH_2O + M' \rightarrow HCO + H + M'$	5.000E+16	0.00	320
34f	$CH_2O + H \rightarrow HCO + H_2$	2.300E+10	1.05	13.7
35f	$CH_2O + O \rightarrow HCO + OH$	4.150E+11	0.57	11.6
36f	$CH_2O + OH \rightarrow HCO + H_2O$	3.400E+09	1.20	−1.9
37f	$CH_2O + HO_2 \rightarrow HCO + H_2O_2$	3.000E+12	0.00	54.7
38f	$CH_3 + O \rightarrow CH_2O + H$	8.430E+13	0.00	0
39f	$CH_3 + H \rightarrow CH_4 \quad k_0$	6.257E+23	−1.80	0
	k_∞	2.108E+14	0.00	0
40	$CH_3 + OH \rightarrow CH_3O + H$	2.260E+14	0.00	64.8
41	$CH_3 + O_2 \rightarrow CH_2O + OH$	3.300E+11	0.00	37.4
42f	$CH_3 + HO_2 \rightarrow CH_3O + OH$	1.800E+13	0.00	0
43f	$CH_3 + HO_2 \rightarrow CH_4 + O_2$	3.600E+12	0.00	0
44	$2CH_3 \rightarrow C_2H_4 + H_2$	1.000E+16	0.00	134
45f	$2CH_3 \rightarrow C_2H_6 \quad k_0$	1.272E+41	−7.00	11.6
	k_∞	1.813E+13	0.00	0
46f	$CH_3O + M' \rightarrow CH_2O + H + M'$	5.000E+13	0.00	105
47f	$CH_3O + H \rightarrow CH_2O + H_2$	1.800E+13	0.00	0
48f	$CH_3O + O_2 \rightarrow CH_2O + HO_2$	4.000E+10	0.00	8.9
49f	$CH_2OH + M' \rightarrow CH_2O + H + M'$	5.000E+13	0.00	105
50f	$CH_2OH + H \rightarrow CH_2O + H_2$	3.000E+13	0.00	0
51f	$CH_2OH + O_2 \rightarrow CH_2O + HO_2$	1.000E+13	0.00	30
52f	$CH_4 + H \rightarrow H_2 + CH_3$	1.300E+04	3.00	33.6
53f	$CH_4 + OH \rightarrow H_2O + CH_3$	1.600E+07	1.83	11.6
54f	$HCCO + H \rightarrow 3\text{-}CH_2 + CO$	1.500E+14	0.00	0
55	$HCCO + O \rightarrow 2CO + H$	9.600E+13	0.00	0
56f	$C_2H_2 + O_2 \rightarrow HCCO + OH$	2.000E+08	1.50	126
57f	$C_2H_2 + O \rightarrow 3\text{-}CH_2 + CO$	1.720E+04	2.80	2.1
58f	$C_2H_2 + O \rightarrow HCCO + H$	1.720E+04	2.80	2.1
59f	$C_2H_3 \rightarrow C_2H_2 + H \quad k_0$	1.187E+42	−7.50	190
	k_∞	2.000E+14	0.00	166
60	$C_2H_3 + O_2 \rightarrow CH_2O + HCO$	5.420E+12	0.00	0
61f	$C_2H_4 + M' \rightarrow C_2H_2 + H_2 + M'$	2.500E+17	0.00	320
62f	$C_2H_4 + H \rightarrow C_2H_3 + H_2$	1.700E+15	0.00	62.9
63f	$C_2H_4 + OH \rightarrow C_2H_3 + H_2O$	6.500E+13	0.00	24.9
64f	$C_2H_5 \rightarrow C_2H_4 + H \quad k_0$	1.000E+16	0.00	126
	k_∞	1.300E+13	0.00	167
65f	$C_2H_5 + H \rightarrow 2CH_3$	3.000E+13	0.00	0
66f	$C_2H_5 + O_2 \rightarrow C_2H_4 + HO_2$	1.100E+10	0.00	−6.3
67	$C_2H_6 + H \rightarrow C_2H_5 + H_2$	1.400E+09	1.50	31.1
68	$C_2H_6 + OH \rightarrow C_2H_5 + H_2O$	7.200E+06	2.00	3.6
69	$C_2H_6 + CH_3 \rightarrow C_2H_5 + CH_4$	1.500E−07	6.00	25.4
70	$C_3H_4 + OH \rightarrow CH_2O + C_2H_3$	1.000E+12	0.00	0
71	$C_3H_4 + OH \rightarrow HCO + C_2H_4$	1.000E+12	0.00	0
72f	$C_3H_5 \rightarrow C_3H_4 + H$	3.980E+13	0.00	293
73f	$C_3H_5 + H \rightarrow C_3H_4 + H_2$	5.000E+12	0.00	0
74f	$C_3H_5 + O_2 \rightarrow C_3H_4 + HO_2$	6.000E+11	0.00	41.9
75f	$C_3H_6 \rightarrow C_2H_3 + CH_3$	3.150E+15	0.00	359
76f	$C_3H_6 + H \rightarrow C_3H_5 + H_2$	5.000E+12	0.00	6.3
77f	$C_3H_6 + OH \rightarrow C_2H_5 + CH_2O$	7.900E+12	0.00	0
78f	$C_3H_6 + OH \rightarrow C_3H_5 + H_2O$	4.000E+12	0.00	0
79	$C_3H_6 + CH_3 \rightarrow C_3H_5 + CH_4$	8.960E+12	0.00	35.6
80f	$N\text{-}C_3H_7 \rightarrow CH_3 + C_2H_4$	9.600E+13	0.00	130
81f	$N\text{-}C_3H_7 \rightarrow H + C_3H_6$	1.250E+14	0.00	155
82f	$N\text{-}C_3H_7 + O_2 \rightarrow C_3H_6 + HO_2$	1.000E+12	0.00	20.9

(*continued on next page*)

Appendix A (*Continued*)

Number	Reaction	A	n	E
83f	$1\text{-}C_4H_8 \rightarrow C_3H_5 + CH_3$	8.000E+16	0.00	307
84f	$1\text{-}C_4H_8 + OH \rightarrow N\text{-}C_3H_7 + CH_2O$	6.500E+12	0.00	0
85	$P\text{-}C_4H_9 \rightarrow C_2H_5 + C_2H_4$	2.500E+13	0.00	121
86	$1\text{-}C_5H_{11} \rightarrow C_2H_4 + N\text{-}C_3H_7$	3.200E+13	0.00	119
87	$C_6H_{11} \rightarrow C_3H_5 + C_3H_6$	2.500E+13	0.00	126
88	$1\text{-}C_6H_{12} \rightarrow N\text{-}C_3H_7 + C_3H_5$	2.500E+16	0.00	298
89	$1\text{-}C_6H_{12} + H \rightarrow C_6H_{11} + H_2$	5.000E+12	0.00	0
90	$1\text{-}C_6H_{12} + OH \rightarrow C_6H_{11} + H_2O$	5.000E+12	0.00	0
91	$1\text{-}C_7H_{15} \rightarrow 1\text{-}C_5H_{11} + C_2H_4$	2.500E+13	0.00	121
92	$2\text{-}C_7H_{15} \rightarrow P\text{-}C_4H_9 + C_3H_6$	1.600E+13	0.00	118
93	$2\text{-}C_7H_{15} \rightarrow 1\text{-}C_6H_{12} + CH_3$	4.000E+13	0.00	138
94	$1\text{-}C_7H_{15} \rightarrow 2\text{-}C_7H_{15}$	2.000E+11	0.00	75.8
95	$2\text{-}C_7H_{15} \rightarrow 1\text{-}C_7H_{15}$	3.000E+11	0.00	88.4
96	$N\text{-}C_7H_{16} \rightarrow P\text{-}C_4H_9 + N\text{-}C_3H_7$	3.160E+16	0.00	339
97	$N\text{-}C_7H_{16} + H \rightarrow 1\text{-}C_7H_{15} + H_2$	7.300E+07	2.00	32.2
98	$N\text{-}C_7H_{16} + H \rightarrow 2\text{-}C_7H_{15} + H_2$	3.500E+07	2.00	20.9
99	$N\text{-}C_7H_{16} + OH \rightarrow 1\text{-}C_7H_{15} + H_2O$	1.056E+10	1.10	7.6
100	$N\text{-}C_7H_{16} + OH \rightarrow 2\text{-}C_7H_{15} + H_2O$	5.200E+09	1.30	2.9
101	$N\text{-}C_7H_{16} + HO_2 \rightarrow 1\text{-}C_7H_{15} + H_2O_2$	1.790E+13	0.00	81.2
102	$N\text{-}C_7H_{16} + HO_2 \rightarrow 2\text{-}C_7H_{15} + H_2O_2$	1.340E+13	0.00	71.2
103	$N\text{-}C_7H_{16} + O_2 \rightarrow 1\text{-}C_7H_{15} + HO_2$	5.500E+13	0.00	205
104	$N\text{-}C_7H_{16} + O_2 \rightarrow 2\text{-}C_7H_{15} + HO_2$	8.000E+13	0.00	199
105f	$1\text{-}C_7H_{15} + O_2 \rightarrow RO_2$	2.000E+12	0.00	0
105b	$RO_2 \rightarrow 1\text{-}C_7H_{15} + O_2$	1.750E+15	0.00	117
106f	$2\text{-}C_7H_{15} + O_2 \rightarrow RO_2$	2.000E+12	0.00	0
106b	$RO_2 \rightarrow 2\text{-}C_7H_{15} + O_2$	1.750E+15	0.00	117
107	$RO_2 \rightarrow R'O_2H$	6.000E+11	0.00	85.6
108	$R'O_2H + O_2 \rightarrow O_2R'O_2H$	5.000E+11	0.00	0
109	$O_2R'O_2H \rightarrow HO_2R''O_2H$	2.000E+11	0.00	71.2
110	$HO_2R''O_2H \rightarrow OR''O_2H + OH$	1.000E+09	0.00	31.4
111	$OR''O_2H \rightarrow OR''O + OH$	8.400E+14	0.00	180
112	$OR''O \rightarrow CH_2O + 1\text{-}C_5H_{11} + CO$	2.000E+13	0.00	62.8

Units are mole, cubic centimeter, second, kilojoule, Kelvin.

Third body collision efficiencies are $[M'] = 3.0[n\text{-}C_7H_{16}] + 1.0[H_2] + 0.75[CO] + 0.40[N_2] + 6.5[H_2O] + 0.4[O_2]$.

For those rate constants k, which depend on the pressure, k_0 and k_∞ are given in the table and $k = Fk_0[M]/(k_\infty + k_0[M])$, where $\log_{10} F = \log_{10} F_c/(1 + (\log_{10}(k_0[M]/k_\infty)/\hat{N})^2)$ and $\hat{N} = 0.75 - 1.27\log_{10} F_c$.

Broadening functions are given by $F_{c39} = 0.577\exp(-T/2370\ \text{K})$, $F_{c45} = 0.38\exp(-T/73\ \text{K}) + 0.62\exp(-T/1180\ \text{K})$, $F_{c59} = 0.35$, and $F_{c64} = 0.411\exp(-73.4\ \text{K}/T) + \exp(-T/422.8\ \text{K})$.

References

[1] H.K. Ciezki, G. Adomeit, Combust. Flame 93 (4) (1993) 421–433.

[2] R. Minetti, M. Carlier, M. Ribaucour, E. Therssen, L.R. Sochet, Combust. Flame 102 (3) (1995) 298–309.

[3] H.J. Curran, P. Gaffuri, W.J. Pitz, C.K. Westbrook, Combust. Flame 114 (1–2) (1998) 149–177.

[4] C.K. Westbrook, Proc. Combust. Inst. 28 (2000) 1563–1577.

[5] P. Dagaut, M. Reuillon, M. Cathonnet, Combust. Flame 101 (1–2) (1995) 132–140.

[6] N. Peters, G. Paczko, R. Seiser, K. Seshadri, Combust. Flame 128 (1–2) (2002) 38–59.

[7] J.F. Griffiths, P.A. Halfordmaw, C. Mohamed, Combust. Flame 111 (4) (1997) 327–337.

[8] J.F. Griffiths, P.A. Halfordmaw, D.J. Rose, Combust. Flame 95 (3) (1993) 291–306.

[9] C.V. Callahan, T.J. Held, F.L. Dryer, R. Minetti, M. Ribaucour, L.R. Sochet, T. Faravelli, P. Gaffuri, E. Ranzi, Proc. Combust. Inst. 26 (1996) 739–746.

[10] R. Minetti, M. Carlier, M. Ribaucour, E. Therssen, L.R. Sochet, Proc. Combust. Inst. 26 (1996) 747–753.

[11] A. Cox, J.F. Griffiths, C. Mohamed, H.J. Curran, W.J. Pitz, C.K. Westbrook, Proc. Combust. Inst. 26 (1996) 2685–2692.

[12] A. Liñán, A. Crespo, Combust. Sci. Technol. 14 (1976) 95–117.

[13] J.D. Mellado, A.L. Sánchez, J.S. Kim, A. Liñán, Combust. Theory Modeling 4 (3) (2000) 265–288.

[14] J.D. Blouch, C.K. Law, Proc. Combust. Inst. 28 (2000) 1679–1686.

[15] R. Seiser, H. Pitsch, K. Seshadri, W.J. Pitz, H.J. Curran, Proc. Combust. Inst. 28 (2000) 2029–2037.

[16] S. Sreedhara, K.N. Lakshmisha, Proc. Combust. Inst. 28 (2000) 25–34.

[17] S. Schnaubelt, O. Moriue, T. Coordes, C. Eigenbrod, H.J. Rath, Proc. Combust. Inst. 28 (2000) 953–960.
[18] H. Pitsch, N. Peters, SAE Paper No. 982464, 1998.
[19] V. Gopalakrishnan, J. Abraham, Combust. Flame, submitted for publication.
[20] C. Chevalier, P. Louessard, U.C. Müller, J. Warnatz, in: International Symposium on Diagnostics and Modeling of Combustion in Internal Engines COMODIA 90, The Japan Society of Mechanical Engineers, Kyoto, 1990.
[21] D.L. Baulch, C.J. Cobos, R.A. Cox, C. Esser, P. Frank, T. Just, J.A. Kerr, M.J. Pilling, J. Troe, R.W. Walker, J. Warnatz, J. Phys. Chem. Ref. Data 21 (3) (1992) 411–734.
[22] D.L. Baulch, C.J. Cobos, R.A. Cox, P. Frank, G. Hayman, T. Just, J.A. Kerr, T. Murrells, M.J. Pilling, J. Troe, R.W. Walker, J. Warnatz, Combust. Flame 98 (1–2) (1994) 59–79.
[23] R.T. Pollard, in: C.H. Bamford, C.F.H. Tipper (Eds.), Gas-Phase Combustion, vol. 17, Elsevier, Amsterdam, 1977.
[24] S.W. Benson, Prog. Energy Combust. Sci. 7 (2) (1981) 125–134.
[25] M. Bollig, H. Pitsch, J.C. Hewson, K. Seshadri, Proc. Combust. Inst. 26 (1996) 729–737.
[26] R.A. Cox, J.A. Cole, Combust. Flame 60 (2) (1985) 109–123.
[27] T.J. Held, A.J. Marchese, F.L. Dryer, Combust. Sci. Technol. 123 (1–6) (1997) 107–146.
[28] R. Seiser, L. Truett, D. Trees, K. Seshadri, Proc. Combust. Inst. 27 (1998) 649–657.
[29] H.G. Im, L.L. Raja, R.J. Kee, A.E. Lutz, L.R. Petzold, OPUS: A Fortran program for unsteady opposed-flow flames, Technical Report SAND2000-8211, Sandia National Laboratories, 2000.
[30] A.E. Lutz, R.J. Kee, J.F. Grcar, F.M. Rupley, OPPDIF: A Fortran program for computing opposed-flow diffusion flames, Technical Report SAND96-8243, Sandia National Laboratories, 1996.
[31] R.J. Kee, F.M. Rupley, J.A. Miller, Chemkin II: A Fortran chemical kinetics packages for the analysis of gas-phase chemical kinetics, Technical Report SAND89-8009B, Sandia National Laboratories, 1991.
[32] F.A. Williams, Combustion Theory, Perseus Books, 1985, pp. 576–581.
[33] R.W. Bilger, Proc. Combust. Inst. 22 (1988) 475–488.
[34] J.S. Kim, F.A. Williams, J. Eng. Math. 31 (2–3) (1997) 101–118.
[35] T. Niioka, Proc. Combust. Inst. 18 (1981) 1807–1824.
[36] B. Higgins, D. Siebers, SAE Technical Paper No. 2000-01-0940, 2000.